Improving the Laser Powder Bed Fusion Processability of A2618 alloy: Investigation on TiB2 Addition Strategies via Single Scan Track Approach

Journal of Materials Research and Technology 35 (2025) 5175–5189

Contents lists available at ScienceDirect

Journal of Materials Research and Technology

journal homepage: www.elsevier.com/locate/jmrt

Improving the laser powder bed fusion processability of A2618 alloy: Investigation on TiB_2 addition strategies via single scan track approach

Michele Rosito [a,*], Elisa Padovano [a], Stefano Felicioni [a], Matteo Vanzetti [a], Riccardo Casati [b], Joel Larsson [c], Federica Bondioli [a,d]

[a] Department of Applied Science and Technology, Politecnico di Torino, Corso Duca degli Abruzzi 24, 10129 Turin, Italy
[b] Department of Mechanical Engineering, Politecnico di Milano, Via G. La Masa 34, 20156 Milano, MI, Italy
[c] European Space Agency (ESA), Keplerlaan 1, 2200 AG Noordwijk, the Netherlands
[d] Consorzio Interuniversitario Nazionale per la Scienza e Tecnologia dei Materiali (INSTM), Via G. Giusti 9, 50121 Firenze, Italy

A B S T R A C T

Processing aluminum alloys by Laser Powder Bed Fusion (L-PBF) is of great interest for components production in various industries; however, their processability is quite challenging due to their susceptibility to solidification cracking. One effective strategy to overcome this problem is the addition of inoculants to modify their solidification mechanism and to prevent crack initiation. In this context, this study focuses on the processability of the A2618 alloy with the addition of TiB_2 as an inoculant using different *ex situ* strategies: low- and high-energy mechanical mixing and plasma coating respectively. The Single Scan Tracks (SSTs) approach was used to investigate the quality and stability of tracks that greatly influence the quality of printed parts and optimize the process parameters for the three feedstocks. The comparison between the systems enabled the identification of slight differences between powders in terms of the processability window, revealing the influence of the inoculant dispersion method on the processability of the A2618 alloy. Electron Backscatter Diffraction (EBSD) analysis carried out on the SST cross-sections confirmed significant differences between the three powders in terms of grain refinement. In addition to the microstructure refinement and the absence of solidification cracks, the analysis revealed the effectiveness of the plasma coating method which allows for obtaining a uniform and homogeneous distribution of the reinforcement on the aluminum particles' surface. Bulk samples were then produced to validate the optimization study results: the characterization of the cubic samples revealed a dense (99.9%) and crack-free microstructure, with a homogeneous distribution of the reinforcement phase.

1. Introduction

The consolidation of additive manufacturing (AM) processes in the last few decades has been beneficial for various industrial fields [1]. The ability to produce near-net shape parts, lightweight structures, and integrated components [2,3] offers particular advantages, especially in aerospace applications where the production of parts with complex geometries, difficult-to-machine components, and lightweight structures is critical for decreasing costs and emissions [4]. Among the AM processes, Laser-Based Powder Bed Fusion for Metals (PBF-LB/M [5]), known as Laser Powder Bed Fusion (L-PBF), stands out as one of the most widely used techniques to process metallic materials. This is mainly due to the ability to obtain unique microstructures and improve mechanical properties thanks to the high cooling rate involved in the process [6].

Although L-PBF technology is now well-established, the metallic materials suitable for this process remain limited. Certain classes of alloys, such as steel, titanium alloys, and some nickel-based superalloys, are relatively easy to process with L-PBF [7]. In contrast, aluminum alloys pose significant challenges due to their high thermal conductivity, high reflectivity, and poor feedstock flowability. Traditional casting aluminum alloys, such as AlSi10Mg [8–10], AlSi12 [11,12], or AlSi10Mg0.7 [13], were among the first alloys successfully processed by L-PBF. Their relatively high Si content lowers the viscosity of the molten metal and narrows the solidification range, improving their processability [14]. Conversely, L-PBF of wrought aluminum alloys, particularly high-strength aluminum alloys, is demanding. These materials are characterized by poor fluidity, a wide solidification range, and high crack susceptibility [15] due to their columnar dendritic grain growth [16]. Maamoun et al. [17], for instance, performed a process parameters optimization to investigate their influence on the microstructure and mechanical properties of Al6061 alloy. Independently of the used process parameters, the produced samples exhibited solidification cracks that propagated along the building direction. Tan et al. [18] also evaluated the effect of laser power and scanning speed on the L-PBF processability of A2024 alloy, highlighting that hot cracking could be

* Corresponding author. Corso Duca degli Abruzzi 24, 10129, Torino, Italy.
E-mail address: michele.rosito@polito.it (M. Rosito).

https://doi.org/10.1016/j.jmrt.2025.02.167
Received 6 November 2024; Received in revised form 18 February 2025; Accepted 18 February 2025
Available online 20 February 2025

minimized by adopting low (<40 J/mm^3) or high (>140 J/mm^3) volumetric energy density. However, within these process windows, the crack density decreased at the cost of increased porosity.

To enhance the processability of high-strength aluminum alloy for L-PBF, different strategies have been developed, leading to notable improvements in printability. These include increasing the Si content to narrow the solidification range [19–21], preheating the building platform to mitigate thermal gradient [22], and introducing inoculants to modify the solidification mechanism. The introduction of heterogeneous nucleation sites hinders the formation of columnar grains and promotes the growth of equiaxial grains, thereby preventing the initiation and propagation of solidification cracks [23,24]. Furthermore, the use of these inoculant phases (such as Al_3Zr [25,26], $TiAl_3$ [27], TiB_2 [28–31], and TiC [32–34]) can enhance the powder bed absorptivity [32] and improve the mechanical properties of the material through the production of a metal matrix composite with increased Young's modulus, stiffness, and hardness [33]. The consolidation of these strategies, together with the potential offered by the L-PBF process, has led to the development of new compositions specifically designed for this process (ultrahigh-strength Al alloys) [34,35], with the potential to achieve mechanical properties significantly superior to those of traditional Al alloys.

The design and production of Aluminum Matrix Composites (AMCs) can be carried out using various strategies, such as blending the reinforcement particles with the Al powder (*ex situ*) or synthesizing the reinforcement during the L-PBF [36] or gas atomization [37] (*in situ)*. While *in situ* particles offer a strong interfacial bonding, their synthesis is challenging because of the control of the reactions in terms of unreacted precursors and synthesized phases [27,38,39]. Conversely, *ex situ* reinforcements may require additional effort to achieve a homogeneous distribution and a stronger bond with the matrix but are simpler to design and implement and often come with lower costs.

In this work, the processability of the high-strength 2618 Al alloys was investigated and improved through the addition of inoculant phases. This alloy belongs to 2XXX high-strength aluminum alloy class and finds widespread application in the automotive and aerospace industries due to its ability to preserve good mechanical properties at temperatures up to 300 °C [40]. However, its processability for L-PBF is limited due to its susceptibility to hot cracking. Various attempts have been made to enhance the printability of this alloy by incorporating inoculant phases and producing AMCs [25]. Belelli et al. [41,42] reported that TiB_2 is highly effective both as a grain refiner and for improving the mechanical properties of the material [38,39]. However, to the authors' knowledge, only the pre-alloying strategy has been employed to incorporate TiB_2 particles in the matrix.

This work aims to investigate the influence of TiB_2 addition on the processability of A2618 alloy by L-PBF by adopting different reinforcement addition strategies. In particular, three different technologies to obtain A2618 AMC were studied and compared: (i) low-energy and (ii) high-energy mechanically mixed A2618 and TiB_2 [43], and (iii) TiB_2--coated A2618 [24]. To evaluate the powder processability by L-PBF, the single scan track (SSTs) approach [44,45] was adopted to optimize the process parameters. The analysis of the obtained SSTs in terms of both cross-section and on-top morphologies, in fact, enabled the determination of the most promising values of power and scanning speed in processing these materials. Based on these results, massive samples were produced to evaluate their densification degree.

2. Materials and methods

2.1. Powders characterization

In this work, three different composite powders of A2618 alloy reinforced with 5 vol% TiB_2, in addition to the standard A2618 alloy, were investigated (Table 1). The choice of A2618 alloy and TiB_2 as the matrix and reinforcement, respectively, for the AMC was made after a comparison of different Al alloys and ceramic phases, taking into account several properties (such as microstructural stability, mechanical and thermal properties, high-temperature performance, and reactivity). Based on these comparisons, the combination A2618/TiB_2 proved to be the most suitable for this work. The three systems differ in the *ex-situ* methods adopted for dispersing TiB_2 particles in the Al-based matrix. Powder B was obtained by low-energy mechanical mixing, using a low-energy drums mixer under Ar atmosphere at 40 rpm for 2 h; powder C was obtained by high-energy mechanical mixing under N_2 atmosphere; finally, powder D was obtained by plasma coating through non-thermal plasma glow discharge [46].

Table 1
Investigated powder systems.

Label	Description	supplier
A	Standard A2618 alloy	Kymera International GmbH (Velden, Germany)
B	Low-energy mechanically mixed A2618 + TiB_2	A2618: Kymera International GmbH (Velden, Germany) TiB_2: Höganäs SA (Höganäs, Sweden)
C	High-energy mechanically mixed A2618 + TiB_2	IMR GmbH (Lind ob Velden, Austria)
D	Plasma Coated A2618 + TiB_2	AM4AM S.à r.l. (Foetz Mondercange, Luxemburg)

The powders were first characterized to highlight the differences in terms of morphology, particle size distribution [47], and flowability as influenced by the different preparation methods. The granulometry of the powders was evaluated using a laser diffraction particle size analyzer Mastersizer 3000 (Malvern Panalytical, Malvern, UK). The morphology and chemical composition of the particles were investigated through scanning electron microscopy, using a Phenom ProX SEM (Thermo Fisher Scientific, Waltham, MA, USA) equipped with an EDS detector. Low-magnification micrographs of the powders were acquired to estimate the aspect ratio (AR) and circularity of the particles through image analysis using the open-access software ImageJ (Wayne Rasband, Bethesda, MD, USA). The flow behavior and the spreadability of the powders were investigated through powder flow tests conducted with an FT4 Powder Rheometer (Freeman Technology Ltd, Tewkesbury, UK). Finally, the absorbance of the powders was evaluated using a UV–Vis spectrophotometer UV-2600 (Shimadzu, Kyoto, Japan) equipped with an integration sphere ISR-2600Plus, in diffuse reflectance mode between 220 and 1350 nm.

2.2. Single scan tracks production

With the aim of investigating the processability of the three composite powders by Laser Powder Bed Fusion (L-PBF), a Single Scan Tracks (SSTs) approach was used. The SST samples were produced using a Print Sharp 250 (Prima Additive, Torino, Italy), a medium-volume (258 × 258 × 330 mm^3) L-PBF machine equipped with a 500 W single-mode IR fiber laser emitting at a wavelength of 1070 nm.

A total of four jobs were manufactured for each powder. The first two jobs were produced to evaluate the influence of laser power (P) and scanning speed (v) on the processability of the investigated materials within a wide process window. In these jobs, P ranged from 250 to 450 W with increments of 50 W, while v varied from 200 to 1800 mm/s with a step of 200 mm/s, resulting in a total of 54 tracks produced for each system. Subsequently, a third job was manufactured to investigate the effect of the two parameters within a narrower process window, based on the results obtained from the characterization of the previous jobs. In this third job, P varied in the range between 350 and 425 W, while v ranged from 1100 to 1700 mm/s.

The SSTs were printed on A2618 discs used as substrates, following the design depicted in Fig. 1a (an example of the printed samples is shown in Fig. 1b). The powder layers were spread using a film depositor with a 60 μm gap. The layer thickness was chosen based on the results

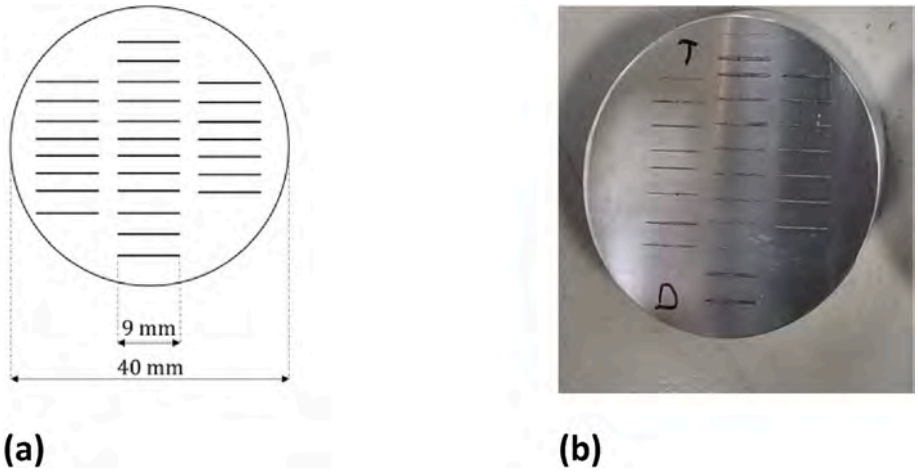

Fig. 1. (a) Schematic representation of the produced jobs, and (b) an example of SSTs samples.

carried out by Mindt et al. [48]. In their study, they observed that, in the initial stages of the L-PBF process, the real powder bed thickness increases until it reaches a steady-state value. This behavior is related to the shrinkage of the previous layers: in fact, during the consolidation of the first layers, the powder melting results in a consolidated layer with a real thickness lower than the theoretical one (set by slicing and equal to the vertical displacement of the platform during the L-PBF process). This reduction in thickness is due partly to the apparent density of the powder and the presence of voids between the particles, and partly to the thermal shrinkage as the molten metal cools. The subsequent layer will then have a thickness equal to the set layer thickness (t), increased by a δz to account for the shrinkage of the previous layer. Furthermore, they noted that this steady-state value is generally twice the set layer thickness and corresponds to the platform displacement. For aluminum alloys processed with the Print Sharp 250, a nominal layer thickness of 30 μm was generally used, corresponding to a steady-state value of 60 μm. To ensure a homogeneous powder bed on the substrates, a slurry consisting of powder and ethanol (50 vol%) was used to facilitate the spreading of the layers. Before printing the tracks, the ethanol was allowed to evaporate in the building chamber at room temperature for 1 h, under Ar flow.

2.3. Single scan tracks characterization

The SSTs were characterized in terms of their on-top profile and cross-section. The on-top analysis was carried out on the first two jobs to identify a stability range within the investigated process parameters window. An optical microscope Leica DMI 5000 M (Leica Microsystems, Wetzlar, Germany) was used to acquire images of the tracks along their entire length. For each track, the different micrographs were stitched together to form an image of the complete track. These images were first subjected to visual examination to identify tracks showing discontinuities that could not be considered for further analyses. Subsequently, the continuous tracks were post-processed using MATLAB software previously developed to assess their stability through the definition of quantitative parameters. Based on existing literature on SSTs [44,45,49,50], the average track width (P1), its standard deviation (P2), and the track roughness (P3) were selected for the analysis. The average track width (P1) was used to assess the influence of process parameters (such as laser power P and scanning speed v) on the track width. The second parameter was the width standard deviation index (P2) based on Equation (1):

$$P2 = \sqrt{\frac{\sum_{i=1}^{N} (x_i - \bar{x})^2}{N}} \quad \text{(Equation 1)}$$

where x_i is the track width in the i-point, $\bar{x}$ is the average track width, and N is the number of points considered along the track length. To define P2, 100 points were considered for each track.

The third parameter was the roughness index (P3), defined according to Equation (2):

$$P3 = \frac{\sum_n h_{peak} - \sum_n h_{valley}}{n} \quad \text{(Equation 2)}$$

where h_{peak} and h_{valley} are the heights of the n-peak and n-valley, respectively, and n is the number of peaks and valleys considered. To define P3, five peaks and valleys were considered for each track. The analysis of P2 and P3 enabled the evaluation of track stability by assessing the presence of defects along its entire length.

The analysis of the cross-sections was conducted on the third job, produced using a narrower range of parameters. To investigate the cross-sections, the disks were cut, mounted, and polished following the standard metallographic procedure. The samples were then etched using Keller's solution for 15 s to highlight the meltpool boundaries. A micrograph for each cross-section was acquired using the optical microscope to measure the geometrical parameters of the meltpools (growth, g, and depth, d), which are schematized in Fig. 2.

For each powder, the cross-section obtained with the optimal process parameters set was analyzed with a focused ion beam scanning electron microscope (FIB-SEM, TESCAN S9000G, Tescan Company, Brno, Czech Republic) equipped with an electron backscatter diffraction (EBSD) analyzer to evaluate the effectiveness of grain refinement in relation to the dispersion method adopted. The analysis was carried out at 20 kV and 10 A, with a step size of 0.5 μm.

2.4. Cubic samples production and characterization

A job consisting of cubic samples was produced to evaluate the densification behavior of the different systems. For each powder, ten cubic samples, each measuring 10 × 10 × 10 mm^3, were printed, using a hatching distance of 160 μm, a layer thickness of 30 μm [51,52], laser powers of 375 and 400 W, and a scanning speed ranging from 1200 to

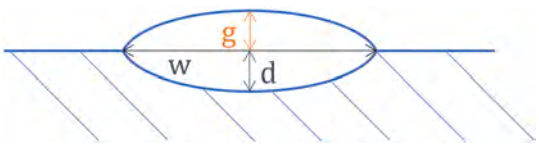

Fig. 2. Geometrical parameters of the meltpool: growth g, depth d, and width w.

1600 mm/s.

The cubes were removed from the platform using an electrical discharge machine (EDM) and were roughly polished to eliminate surface roughness. The density of the samples was evaluated using Archimedes' method. Image analysis was used on the samples to validate the obtained results (for each sample, 15 images were acquired using the optical microscope at 10X) and evaluate the presence of process defects.

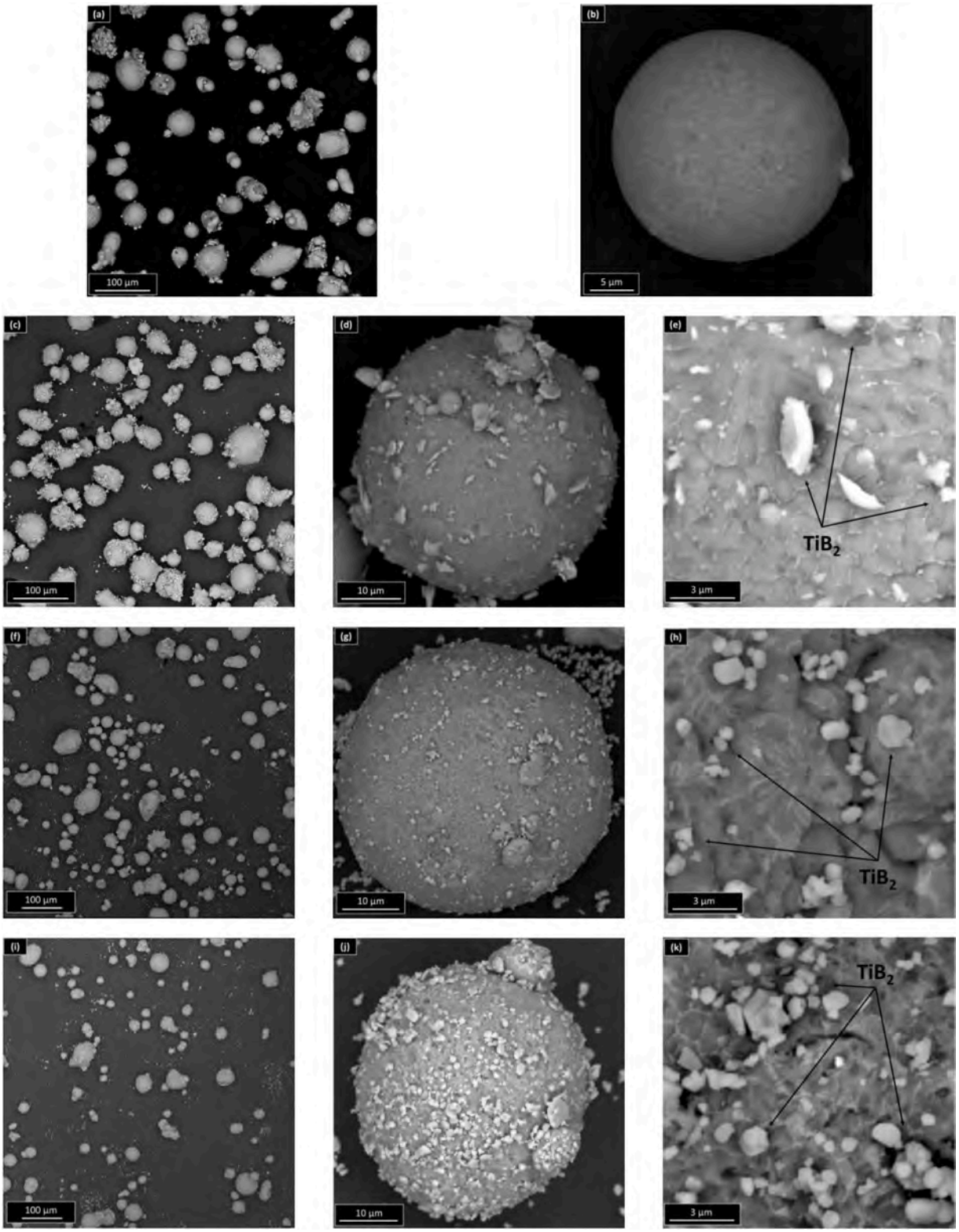

Fig. 3. SEM BSD micrographs of (a–b) A2618, (c–e) low-energy mechanically mixed A2618 + TiB_2, (f–h) high-energy mechanically mixed A2618 + TiB_2, and (i–k) plasma-coated A2618 + TiB_2, at low and high magnification.

3. Results and discussion

3.1. Powders characterization

Micrographs of the different powders can be observed in Fig. 3, while the aspect ratio, circularity, and particle size distribution parameter values are reported in Table 2. In powders B, C, and D, it is easy to distinguish the Al powder, which is the main component, and the TiB_2 particles (identified as such through EDS analysis) dispersed on their surface. For all the systems, it is possible to observe that the particles are predominantly spherical, although the presence of satellites and elongated or irregular particles can be noticed. Examining the geometric parameters of the powders, shown in Table 2, two points are noteworthy: on the one hand, the high standard deviation suggests that the powders consist of a large fraction of irregular particles with nonspherical morphology. On the other hand, there are no significant changes in aspect ratio and circularity in powders B and C: mechanical mixing, conducted at both low and high energy, does not seem to have caused plastic deformation or a worsening of the particle sphericity, as can also be observed by comparing the images of the pure alloy (Fig. 3a and b) with those of powders B (Fig. 3c and d) and C (Fig. 3f and g).

As for the ceramic reinforcement, the TiB_2 particles appear well dispersed on the surface of the Al particles, although agglomerates can be detected in powders C and D. It is also worth noting that, when comparing these feedstocks, the reinforcement appears better dispersed and distributed on the Al particles in the case of powder D, with better adhesion to the surface. Ceramic particles exhibit polygonal and irregular morphology. In addition, the size of these particles in powder B is larger than in the other two, where TiB_2 particles have submicrometric sizes. The use of submicrometric or nanometric particles can be convenient in terms of nucleating effectiveness and mechanical properties [53], but can also cause agglomeration phenomena that can worsen the flowability of the powder [54].

The particle size distributions of the four investigated systems are shown in Fig. 4, while the D10, D50, and D90 values are summarized in Table 2. A significant difference consists of the type of distribution, which is monomodal for powder A, and bimodal for the composite powders. For these powders a low-intensity peak is observable due to the presence of ceramic particles. The position of this peak is in accordance with the morphological observations made by analyzing SEM images of the powder. For powder B, the TiB_2 particles have micrometric size, while for powders C and D, they are submicrometric. These considerations are confirmed by the quantitative parameters of PSD, particularly D10: the latter is lower in composite powders than in powder A due to the presence of TiB_2, and it is minimal in powders C and D.

The flow behavior and the spreadability of the powder feedstocks were evaluated through rheological tests, using an FT4 powder rheometer. The instrument allows for the assessment of the powder behavior under low-intensity stresses, thus simulating the spreading of the powder bed by the recoater [55]. The measured values of basic flowability energy (BFE), specific energy (SE), and conditioned bulk density (CBD) are shown in Fig. 5. The BFE enables the quantification of the energy required to flow a stabilized powder with a certain flow rate and pattern: whereby high BFE values indicate a powder that is difficult to dislocate due to phenomena such as mechanical interlocking and friction. Among the powders, B showed the highest value of BFE, while C and D had the lowest values. The larger size and more irregular morphology of TiB_2 in powder B may contribute to increased inter-particle friction and poorer flowability. Regarding the SE, there are no significant differences between powders. The low values indicate low cohesiveness. Lastly, the CBD allows for evaluating the bulk density of the powder after a conditioning phase. For this reason, high CBD values are desired as they indicate the powder ability to self-arrange and create a compact and dense layer. Among the powders, C has the highest CBD value. It is possible that the larger size of TiB_2 in powder B, and the presence of agglomerates in powder D, increase interparticle friction and hinder the powder self-packing.

In light of these considerations, powder C has the best rheological properties and flowability.

Finally, the absorptivity of each powder was evaluated, and the corresponding spectra are depicted in Fig. 6, along with the absorbance values at 1064 nm (the wavelength of the laser of the PrintSharp 250, the L-PBF machine used in this work). The absorbance of pure A2618 alloy aligns with that of other high-strength Al alloys, such as A7075 and A2219 [56,57], with a value of approximately 53%. It is worth noting that the addition of TiB_2 particles enhanced the absorptivity in all three cases of composite powders (B, C, and D), consistent with previous findings in the literature, where lower reflectivity particles (such as TiO_2 [56], Ti/B_4C [58], TiN [59]) c. Comparing the spectra of powders B and C, both obtained through mechanical mixing, it is possible to note that the absorbance follows a similar trend, although the absorptivity of powder C is slightly higher compared to that of powder B. The different absorption values of these two powders can be explained by considering two aspects: on the one hand, the high-energy mechanical mix leads to a more homogeneous dispersion of the reinforcement on the Al particle surfaces, providing a stronger bond between Al and TiB_2 particles; on the other hand, the TiB_2 size in powder C is significantly smaller than that in powder B, resulting in a larger specific surface area and higher absorptivity [60]. Regarding powder D, the TiB_2-plasma coated powder reveals the highest absorptivity among the investigated systems, with an increment of 7% compared to mechanically mixed powders: the enhanced absorbance can be related to the homogeneous distribution of reinforcement particles along the Al particles (Fig. 3j and k). In addition to the small sizes of ceramic particles, the formation of a uniform TiB_2 coating increases the particle roughness, enhancing their absorptivity [61].

Table 2
Aspect ratio, circularity, and PSD parameters of the selected powders.

	Powder A	Powder B	Powder C	Powder D
Aspect Ratio	1.3 ± 0.4	1.4 ± 0.6	1.2 ± 0.2	1.4 ± 0.5
Circularity	0.6 ± 0.2	0.4 ± 0.1	0.6 ± 0.2	0.7 ± 0.1
D10 (μm)	31.7	27.4	19.1	19.9
D50 (μm)	52.2	49.9	40.8	43.7
D90 (μm)	83.6	89.0	75.4	78.5

3.2. SSTs on-top analysis

The first step of the SSTs characterization consisted of a visual inspection of the tracks. This preliminary step made it possible to recognize tracks with discontinuities or defects. For powder A, SSTs were excluded from the analysis because of the presence of cracks, as can be observed in Fig. 7. In some cases, such as in tracks built with very energetic parameters, cracks were observed along the entire length of the track, while in others they were limited to only a few sections. From Fig. 7c, it can be observed that the crack propagates in the growth direction, as expected from solidification cracks). The presence of centerline cracking aligned with the deposition direction is a well-known phenomenon in conventional welding of high-strength Al alloys [62–66]. In welded Al alloys, cracks originate in the central region of the meltpool and propagate along the welding direction, creating a centerline crack. The propagation along this direction is related both to the growth of columnar grains (in the X–Y plane) along this direction, due to the thermal gradients, and the higher tensile stresses located in this region [67,68].

A similar behavior was observed in Single Scan Tracks (SSTs) produced using aluminum alloys [69,70]. Specifically, Sonawane et al. [69] observed that, in SSTs produced with the A6061 alloy, the cracks preferentially originated from the central part of the meltpool in the presence of high-angle grain boundaries. In order to understand the longitudinal propagation of the crack along the track, the authors

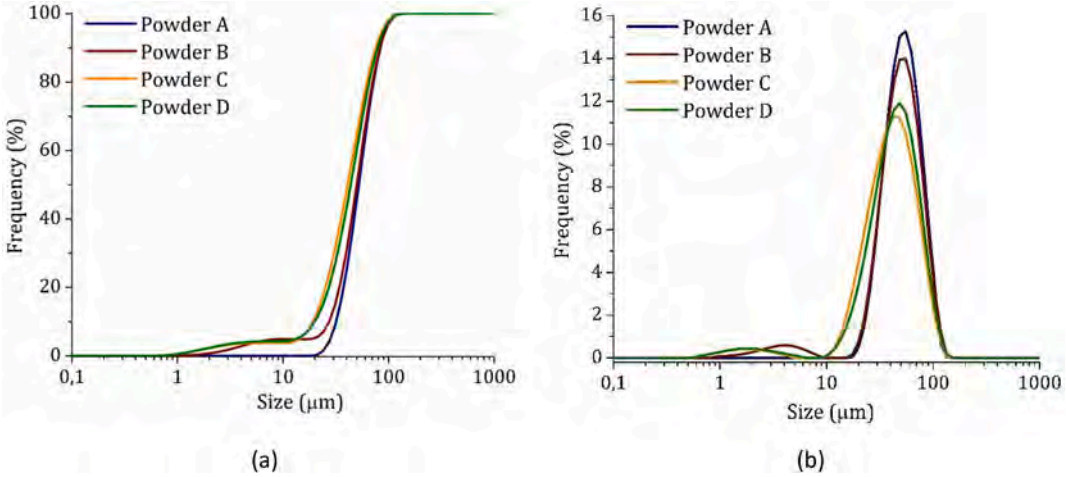

Fig. 4. (a) Frequency and (b) cumulative volume particle size distributions.

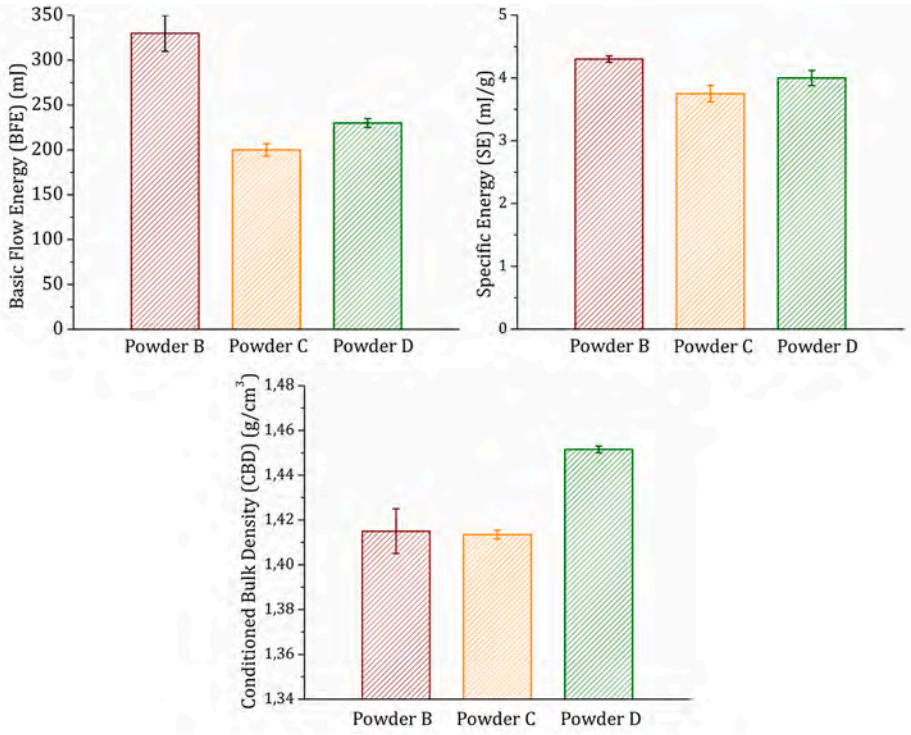

Fig. 5. Basic Flow Energy (BFE), Specific Energy (SE), and Conditioned Bulk Density (CBD) values of the selected powders.

evaluated the length of the mushy zone (in which solidification cracks occur), using it as a cracking sensitivity parameter. The analysis revealed that, at the center of the meltpool and corresponding to the centerline crack, the mushy zone reaches a critical value.

As explained before, this defect is the major limitation to the processability for L-PBF of this type of alloy [23], and its presence compromises the integrity of the component. For this reason, the tracks obtained with powder A were not further characterized.

Visual inspection of the tracks made it possible to recognize discontinuous tracks, which were excluded from the analysis. For instance, in Fig. 8, the on-top surfaces of the SSTs produced with powder B are shown. The SSTs highlighted in red, excluded from further analysis, were produced with combinations of low laser powers and the highest scanning speed that did not provide sufficient energy to enable powder melting.

The continuous tracks were analyzed with MATLAB software to evaluate their thickness and stability and to identify a process window with regular tracks of appropriate width. To select the most promising tracks, the following considerations were made. The first parameter, track width (P1), was considered to evaluate track thickness. Tracks with a width ranging between 216 and 330 μm were deemed acceptable, while widths outside this range were considered unsuitable for the L-PBF process, and the corresponding tracks were excluded. The optimal width range was determined based on the need for overlap between tracks in the bulk samples, and it was calculated according to Equation (3).

$$\varphi = \frac{w-h}{w+h} \bullet 100 \qquad \text{(Equation 3)}$$

where φ is the overlap rate, w is the track width, and h is the hatching distance. The range was calculated considering an overlap between 15 and 35 % [71–73], and a hatching distance of 160 μm. The width standard deviation (P2) and track roughness (P3) were utilized to

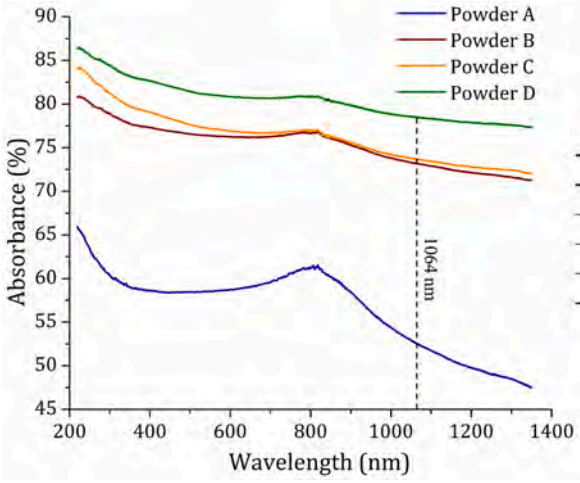

Powder	Absorbance (1064 nm) (%)
Powder A	52,5
Powder B	73,2
Powder C	73,7
Powder D	78,5

Fig. 6. Absorbance spectra and absorbance values at 1064 nm.

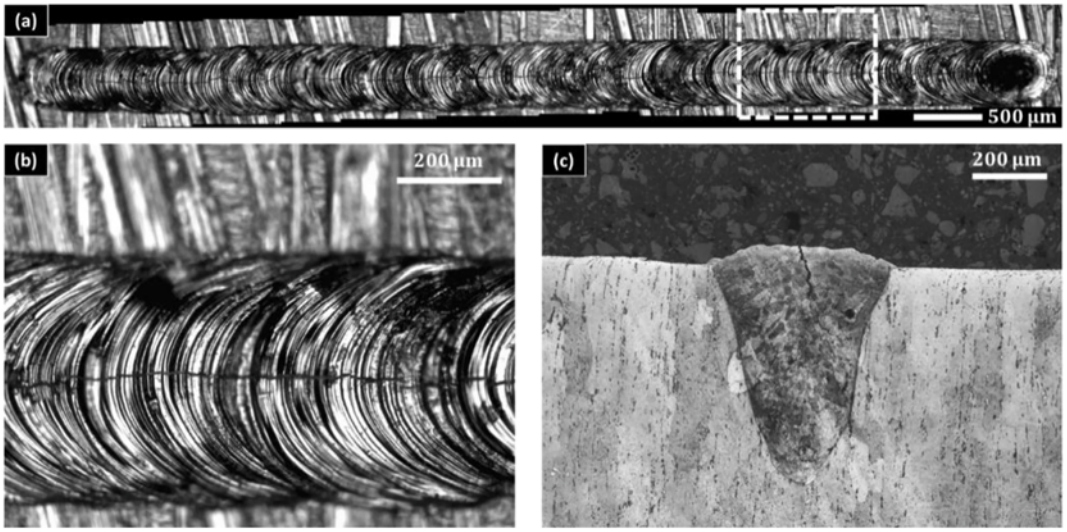

Fig. 7. (a) On-Top surface of the track built with 350 W and 200 mm/s, (b) detail of the surface, and (c) micrograph of the etched cross-section.

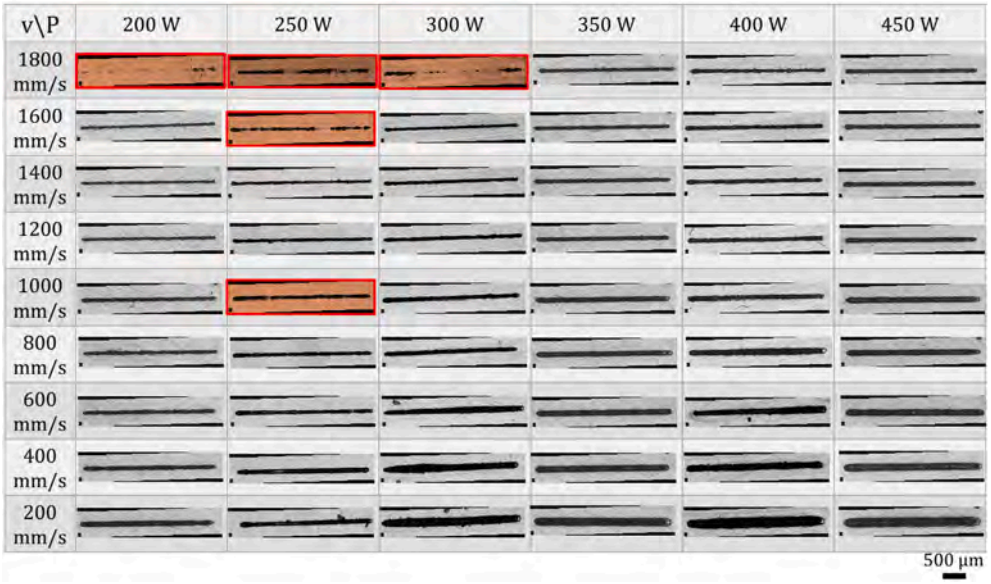

Fig. 8. On-top surfaces of single scan tracks produced with powder B in the first two jobs. Discontinuous tracks are highlighted in red.

describe the regularity and stability of the tracks. High values of P2 would indicate irregular width, track instability, and the presence of defects such as balling. Similarly, high values of P3 would suggest track asymmetry or spattering. Conversely, low values of both P2 and P3 would indicate a regular and stable track. The trends of the three parameters for powder B are shown in Fig. 9. Concerning parameter P1, it is possible to observe that the track width decreases as the scanning speed increases at the same laser power, while the width increases with the increase in laser power. Generally, the track width increases proportionally to the energy supplied to the powder bed, as mentioned in the literature [44,72].

It is interesting to note that both P2 and P3 values are relatively higher when using the highest and lowest scanning speeds for all the considered power values, indicating a higher irregularity of these tracks. Specifically, the use of low scanning speeds (200–600 mm/s) led to the maximum values of P2 and P3, regardless of the laser power applied. In addition to the high width, these tracks show periodic ripples on the surface, which are related to the formation of capillary waves at the interface between the molten alloy and the gas [74]. Conversely, the use of the highest scanning speed leads to the formation of irregular or discontinuous tracks because of insufficient energy and Plateau-Rayleigh capillary instability (as explained by Zheng et al. [75]). In general, intermediate scanning speed, ranging between 800 mm/s and 1400 mm/s, results in lower P2 and P3 values, yielding more regular and stable tracks. Regarding the influence of laser power on material consolidation, it can be observed that low laser powers (such as 200 and 250 W) lead to instability or a small track width. As the laser power increases, these discontinuities disappear, making way for more stable and thicker tracks.

The trends of P1, P2, and P3 for powders C and D are shown in Figs. 10 and 11, respectively. For P1, similar considerations can be drawn for powders C and D as for powder B, with the track width inversely proportional to the energy provided to the powder bed. Besides, it is worth noting that the P1 values for powder C and D are relatively higher with respect to those of powder B, especially for low laser power (between 200 and 300 W). Higher P1 values indicate thicker tracks due to higher energy supplied to the powder bed. Using fine ceramic particles can improve the absorptivity of the powder bed, leading to an increase in the melt pool size [76].

Regarding the P2 parameter, greater instability of the tracks can be observed when using low scanning speeds, which is consistent with what was observed for powder B. Observing the trend of P3, however, it can be noted that for powder D, these values are subject to significant fluctuation, unlike powder C. This variability may suggest a greater instability of the tracks produced with powder D and the convective motions that are generated during the L-PBF process. On the one hand, the fine size of the ceramic particles in this powder can increase the energy absorption of the powder bed, but on the other hand, it can cause the formation of aggregates (observed in Fig. 3i–k), which can increase viscosity and contribute to the track instability.

The integration of considerations regarding the three parameters enabled the development of the process map for powders B, C, and D, as depicted in Fig. 12. These maps allow for summarizing and visualizing the remarks previously made and identify a process window for each powder.

Regarding powder B, for 200 and 250 W, the tracks showed discontinuities or were too small and insufficient in width, because of the low LED used. For 300 W, the tracks were mostly unacceptable, although some regular tracks were obtained for intermediate values of scanning speeds. For laser powers between 350 and 450 W, low scanning speeds led to tracks that were too thick or irregular. However, continuous and stable tracks were identified for scanning speeds ranging from 1000 to 1600 mm/s. In view of these considerations, a process window was identified for laser power between 350 and 450 W, and scanning speeds between 1000 and 1600 mm/s.

The process map for powder C turns out to be similar to that for powder B. Laser powers below 350 W do not allow tracks with a suitable width or sufficient regularity, and the same process window can be identified for laser powers between 350 and 450 W, and scanning speeds between 1000 and 1600 mm/s. For powder D, in contrast to the other investigated systems, higher laser powers and scanning speeds (resulting in lower LED) are required to obtain stable tracks with a suitable width, consistent with the higher absorptivity of the coated powder compared to powders B and C. The process window was found to be between 400

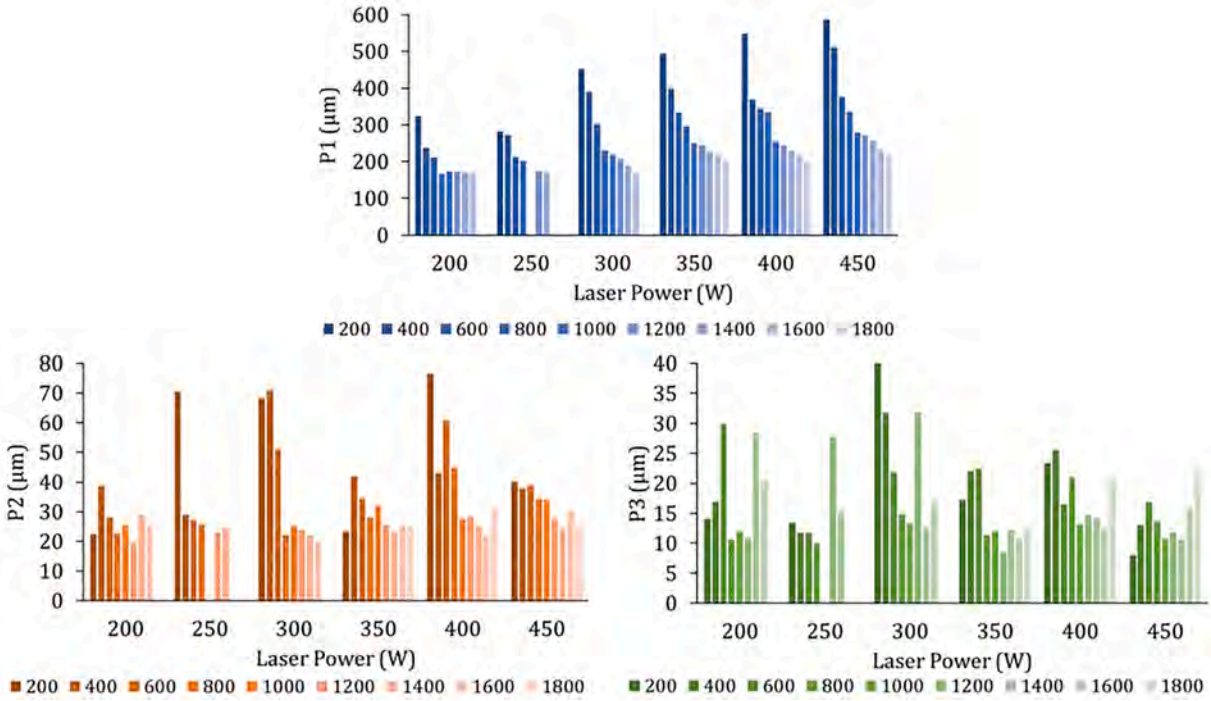

Fig. 9. Track width (P1), width standard deviation (P2), and track roughness (P3) trends for SSTs produced with powder B.

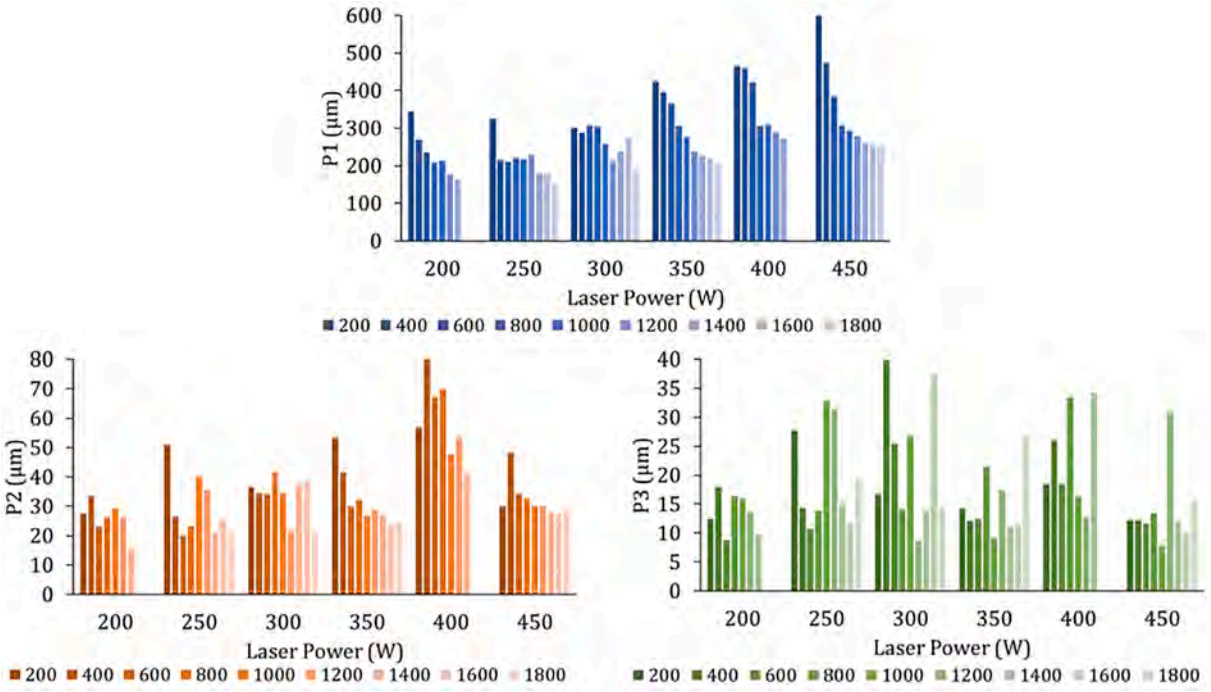

Fig. 10. Track width (P1), width standard deviation (P2), and track roughness (P3) trends for SSTs produced with powder C.

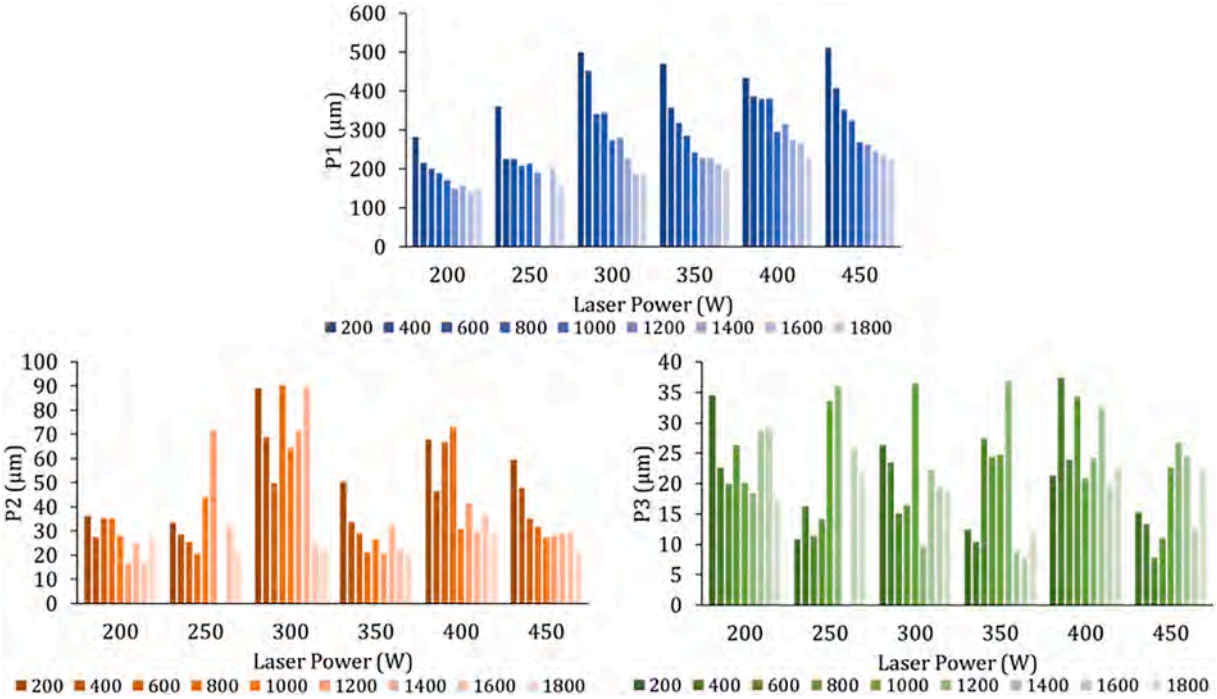

Fig. 11. Track width (P1), width standard deviation (P2), and track roughness (P3) trends for SSTs produced with powder D.

and 450 W for laser power, and scanning speeds above 1000 mm/s.

In general, the three identified process windows are found to fit within the same parameter ranges. To investigate the promising process window in more detail, the third SSTs job was manufactured using a combination of laser powers between 350 and 425 W, with a step of 25 W, and scanning speeds ranging from 1100 to 1700 mm/s, with a step of 100 mm/s.

3.3. SSTs cross-sections analysis

Fig. 13 shows the cross-section micrographs of the SSTs produced in the third job, using a narrower process parameter window. The SSTs highlighted in red were excluded due to the presence of humping and undercuts in the tracks. The presence of these defects is related to the Marangoni flow that arises from surface tension gradients [77] and can lead to the formation of pores and worsen surface roughness in the bulk samples [78–80]. However, it is interesting to note that all cross-sections

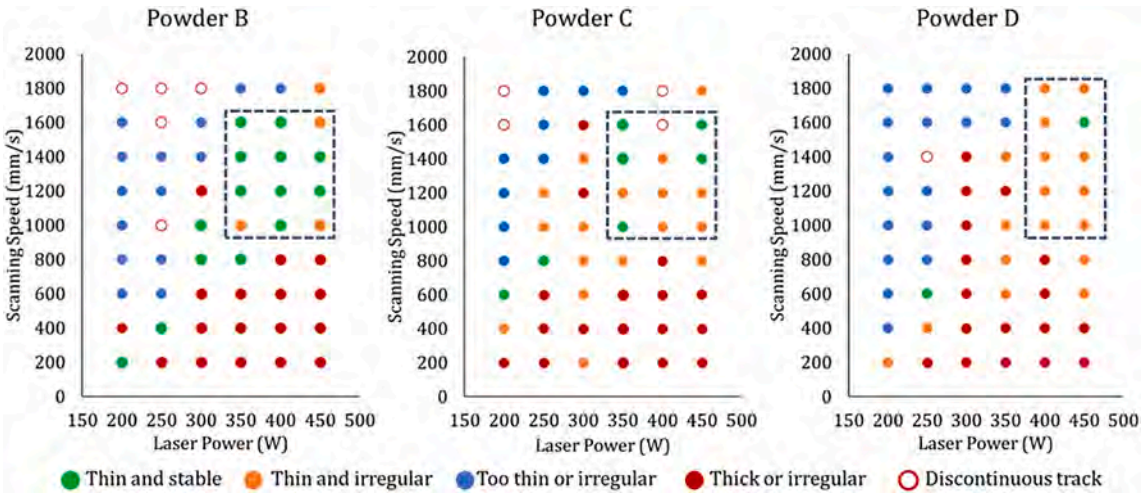

Fig. 12. Process map for powders B, C, and D. The identified process windows are highlighted by the contour.

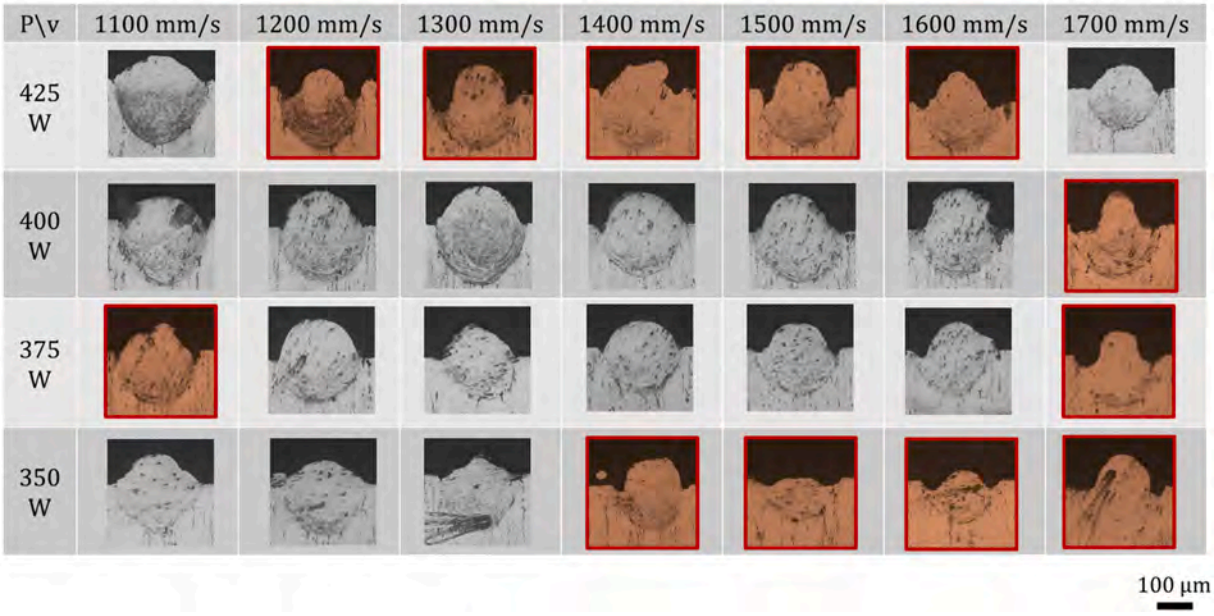

Fig. 13. Cross-section micrographs of the single scan tracks produced with powder B. Excluded tracks are highlighted in red.

were found to be dense and free of solidification cracks: the absence of this defect suggests that the addition of TiB_2 improved the processability of A2618 alloy by modifying its solidification mechanism.

To perform an objective evaluation of the cross-sections and identify a narrower process window, the regular and defect-free melt pools were analyzed in terms of the g/d ratio, where g represents the growth, and d represents the depth of the melt pool. Fig. 14 summarizes the results of this analysis. The use of lower scanning speeds led to melt pools with low g/d ratios and excessive penetration because of the higher energy density provided to the powder bed. Nevertheless, the melt pools obtained using moderate scanning speeds (in a range between 1200 and 1600 mm/s) and laser powers of 375 and 400 W exhibited g/d values between 0.6 and 0.9, which are acceptable and indicate the presence of symmetrical melt pools.

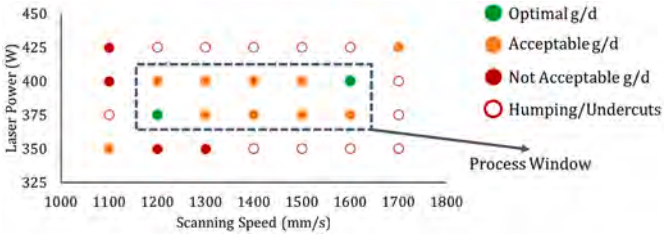

Fig. 14. Process map for powder B. The identified process window is highlighted by the contour.

The results of the cross-section analysis carried out on powders C and D are summarized in Fig. 15, which shows the process maps for these two systems. Similar considerations can be drawn: stable and regular melt pools were obtained using 375 and 400 W as laser powers and intermediate scanning speeds. It is worth noting that the process window for powder D, based on the cross-section analysis, is extremely narrow and limited, confirming the difficulties encountered in processing powder D.

For each powder, a cross-section was selected from the respective process windows and used for EBSD analysis to evaluate the inoculant effect of the TiB_2 particles through the grain morphology and the grain size distribution. The results of these analyses are shown in Fig. 16. Firstly, for powder A (Fig. 16a) it is worth noting the presence of

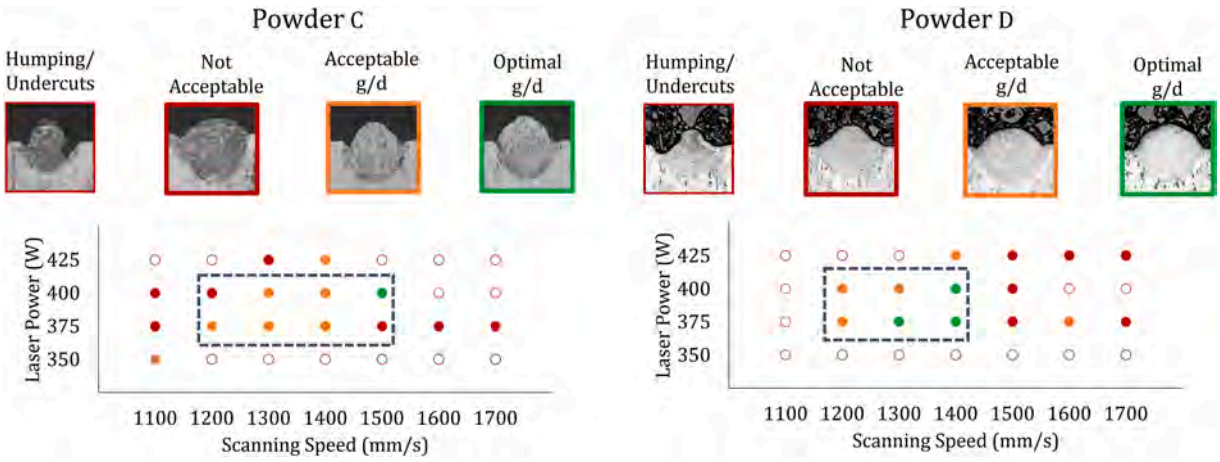

Fig. 15. Process maps for powders C and D. The identified process window is highlighted by the contour.

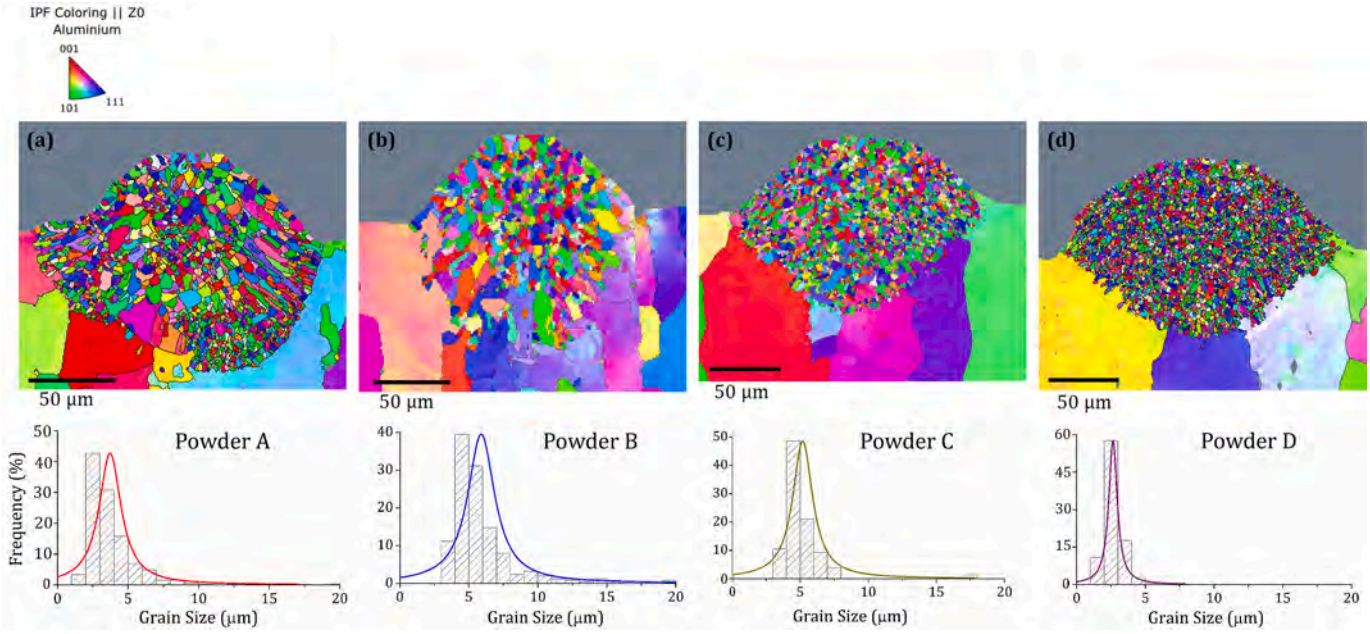

Fig. 16. EBSD analysis of optimal cross-sections and corresponding grain size distributions of powders A (a), B (b), C (d) and D (D).

columnar grains at the melt pool boundary. Alloy 2618 (and, in general, high-strength Al alloys) is subjected to strongly directional solidification during the L-PBF process, so, as expected, the grains tend to grow along the thermal gradient directions [15,81]. At the same time, the formation of columnar grains causes the occurrence of solidification cracks: these cracks can initiate and propagate between the elongated grains due to the difficulty in compensating for solidification shrinkage and accommodating the stresses that arise during solidification. In terms of grain dimensions, the fine size is related to their thin and elongated morphology: this would be confirmed by an aspect ratio of 2.0 ± 0.9, significantly higher than that found for other powders.

Powders B and C (Fig. 16b and c, respectively) allow a comparison of nucleant dispersion carried out by mechanical mixing at different energies. By comparing the EBSD grain maps, it can be noticed that the low-energy mechanical mix leads to partial grain refinement, as columnar grains at the melt pool edge can still be detected. In contrast, the high-energy mechanical mix enables evident grain refinement: the grain size appears to be finer and more regular, and no columnar grains are observed in the melt pool. This is confirmed by the grain size distribution of powder C, which appears to be narrower and left-shifted compared to that of powder B. The greater effectiveness of grain refinement in powder C can have different explanations. On one hand, in powder C the size of TiB_2 particles is much smaller compared to that in powder B, and this can contribute to increasing the effectiveness of the ceramic as a nucleant. At the same time, another aspect to be considered is the impact of the dispersion method. The higher energy used in mechanical mixing would lead to a stronger bond between Al and ceramic particles and ensure better dispersion and distribution of TiB_2 particles. The synergistic action of the size and the distribution might contribute to a more effective grain refinement with respect to powder B.

Powder D (Fig. 16d) is the one that led to the best grain refinement in terms of both grain morphology and grain size. In this case, TiB_2 particles were dispersed in the A2618 powder using a plasma treatment to create a coating. As in powder C, the ceramic particles were also very fine, but they were even more homogeneously dispersed on the surface of the aluminum powders. Comparing the grain size distribution, plasma coating is confirmed to be the most effective dispersion method, with the narrowest curve, shifted to the left among those considered, confirming submicrometric and uniform grain size in the melt pool.

3.4. Cubic samples

The results obtained from both the on-top and cross-section analysis performed on the different powders, led to the selection of the most promising process parameters to be used for printing cubic samples. Cubic samples were therefore produced using laser powers of 375 and 400 W and scanning speeds from 1200 to 1600 mm/s; the residual porosity of the specimens was determined to verify whether the processing window identified for each powder enables the production of dense material.

Fig. 17 shows the porosity trends as a function of process parameters for printed cubic samples. A similar trend can be observed for powders B and D, with an increase in porosity as the scanning speed increases. For powder B, the porosity is constant up to 1400 mm/s and then significantly increases at higher scanning speeds. The lowest porosity value (0.3%) was achieved using a laser power of 375 W and a scanning speed of 1200 mm/s, obtaining a dense sample with homogeneously dispersed ceramic reinforcement. Using higher scanning speeds, defects mainly in the form of cracks were observed in the bulk samples. A further increase in the scanning speed (higher than 1500 mm/s) led to the formation of lack of fusions (LOFs) and the presence of unmelted particles. It is reasonable to suppose that the energy provided to the powder bed was insufficient to melt the powder completely. For powder D, this trend is more marked: the porosity increases significantly as the scanning speed increases; however, a marked difference in terms of densification degree can be observed between the two powers investigated. This would support the considerations regarding the difficult processability of powder D, which were already highlighted from both the on-top (Fig. 12) and cross-sections (Fig. 15) analyses. Regarding the effect of laser power, it can be noticed that the porosity values obtained using 375 W are slightly better compared to those obtained using 400 W, for powders B and D respectively. In contrast, for powder C, the use of 400 W results in slightly better density values. Furthermore, the porosity values were found to be approximately constant and not significantly affected by the scanning speed in the investigated range. Considering that the obtained porosity values are the lowest among the three investigated systems, powder C appears to have the widest process window for producing dense samples.

In Fig. 18, micrographs of cross-sections of samples produced with the three different powders are shown: specifically, cross-sections of the three cubes produced with 375 W and 1200 mm/s are compared. It can be observed that, in all three cases, the ceramic phase appears well distributed in the matrix, although with some differences. As expected, the particle size of TiB_2 is larger in the cube produced with powder B (Fig. 18a) than in those printed with powder C (Fig. 18b) and D (Fig. 18c), respectively. In these cases, the smaller particle size of TiB_2 leads to a more homogeneous and uniform distribution of the ceramic phase in the matrix than in cube B. At the same time, the smaller size of TiB_2 leads to the formation of aggregates, especially in samples produced with powder D (Fig. 18c).

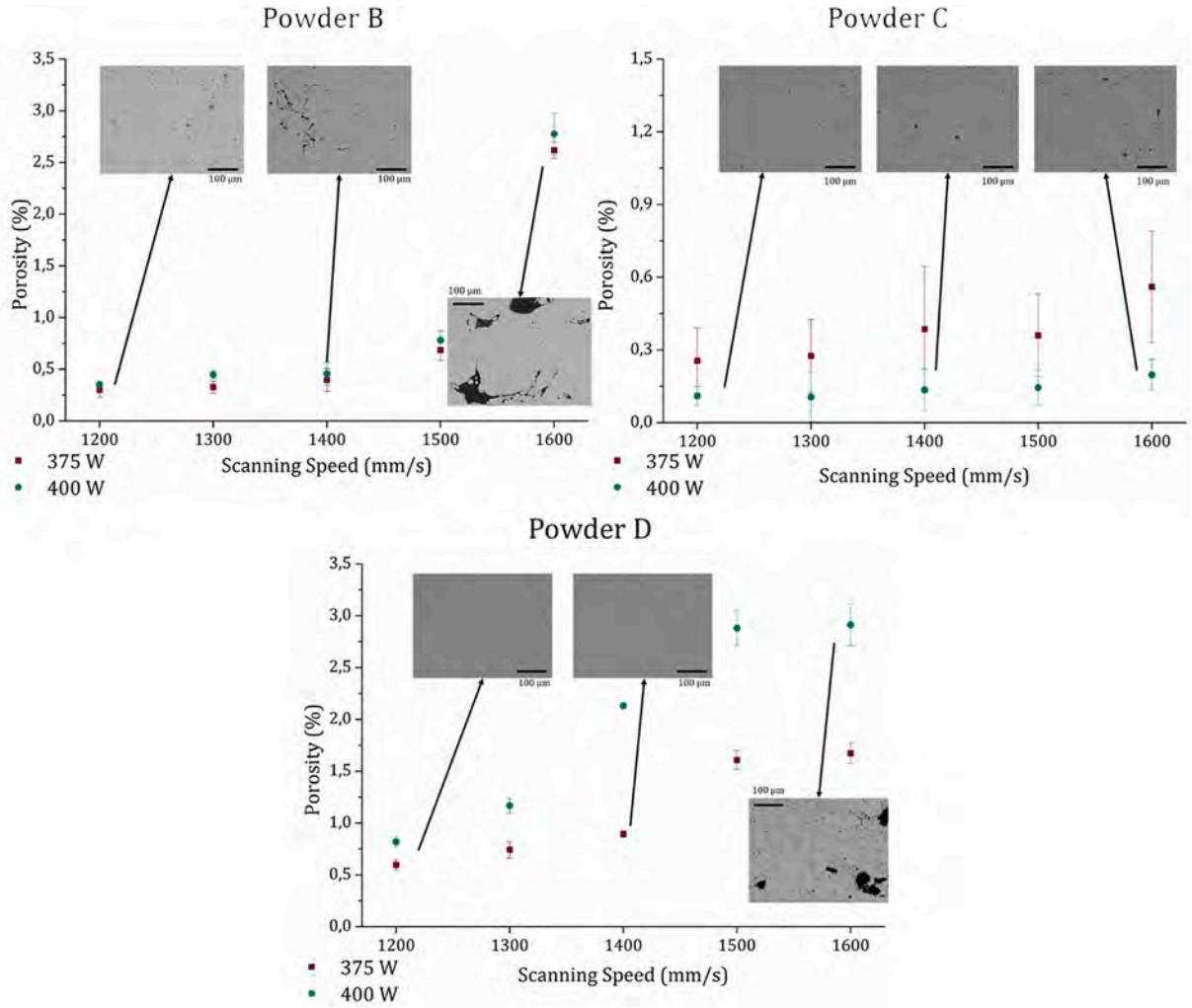

Fig. 17. Porosity values of massive samples produced with powder B, C, and D. Representative micrographs of the cross sections are depicted.

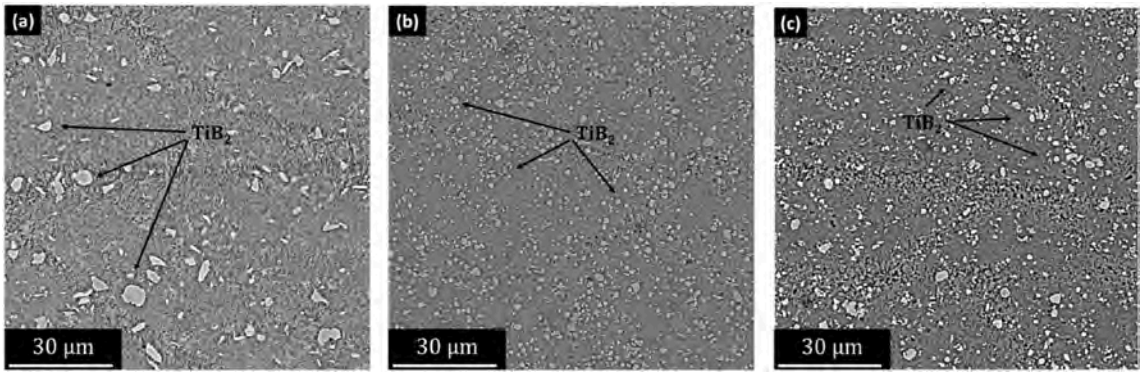

Fig. 18. Backscattered SEM micrographs of the cross sections of the cubic samples printed with 375 W and 1200 mm/s. (a) Powder B, (b) powder C, and (c) powder D.

4. Conclusions

In this work, an investigation of the L-PBF processability of A2618 with the addition of TiB_2 particles as grain refiners was conducted. Three different dispersion methods were considered and investigated, including mechanical mixing performed at both low and high energy, and plasma coating. The SSTs approach was used to carry out a preliminary process optimization, where the processability of the three systems was investigated over a wide range of process parameters, narrowing it down to identify the optimal process window. The effectiveness of the different dispersion systems was evaluated in terms of grain refinement using EBSD analysis. Finally, cubic samples were produced to validate the identified process windows. The following conclusions can be drawn.

1. Both mechanical mixing (at low and high energy) and plasma coating enabled a good dispersion of ceramic particles in the powder without causing deformations to the starting alloy. Generally, using finer TiB_2 particles in powders C and D enabled a more uniform and homogeneous distribution. In terms of flowability, powder C exhibited the best rheological behavior. Finally, the composite powders demonstrated a higher absorptivity compared to pure A2618 powder, confirming the effectiveness of TiB_2 dispersion in enhancing powder absorptivity. In particular, the plasma-coated powder exhibited the highest absorptivity due to the small TiB_2 particle sizes and the increased roughness.
2. In general, for all investigated systems, stable tracks were obtained using scanning speeds between 800 and 1600 mm/s, and laser powers between 350 and 450 W. Lower laser powers (200–300 W) resulted in discontinuous tracks that were not fully fused or were unsuitable in terms of stability and track thickness. Using either low (200–400 mm/s) or excessively high speeds (1800 mm/s) led to melt pool instability, resulting in unsuitable tracks.
3. The analysis of the cross-sections highlighted that, for all three powders, stable melt pools could be obtained with scanning speeds between 1200 and 1600 mm/s, and laser powers of 375 and 400 W, consistent with the process window identified from the on-top analysis. However, powder D proved to be more challenging to process because of the narrower process window compared to powders B and C.
4. The EBSD analysis confirmed that all the considered dispersion methods had a beneficial effect on the processability of alloy 2618 as no solidification cracks were found. However, the three powders showed some significant differences: while low-energy mechanical mixing led to partial grain refinement, this refinement was complete and more effective in powders C and D. In conclusion, plasma coating proved to be the most effective method in terms of both grain size and morphology.
5. The cubic samples revealed high-density values (>99.9%) and the absence of defects. Overall, the SSTs approach proved to be a valid method for conducting preliminary parameter optimization, especially when developing new materials for the L-PBF process.

Funding

The authors acknowledge the European Space Agency (ESA) for funding the Design of Enhanced Metal Matrix Composites for Additive Manufacturing of Space Structures (ENCOMPASS) project.

Declaration of competing interest

The authors declare that they have no known competing financial interests or personal relationships that could have appeared to influence the work reported in this paper.

Acknowledgments

The authors would like to thank BEAMIT SpA for providing A2618 alloy reinforced with TiB_2 powders.

References

[1] Campbell I, Bourell D, Gibson I. Additive manufacturing: rapid prototyping comes of age. Rapid Prototyp J 2012;18:255–8. https://doi.org/10.1108/13552541211231563.
[2] Blakey-Milner B, Gradl P, Snedden G, Brooks M, Pitot J, Lopez E, Leary M, Berto F, du Plessis A. Metal additive manufacturing in aerospace: a review. Mater Des 2021;209. https://doi.org/10.1016/j.matdes.2021.110008.
[3] Najmon JC, Raeisi S, Tovar A. Review of additive manufacturing technologies and applications in the aerospace industry. Additive Manufacturing for the Aerospace Industry 2019:7–31. https://doi.org/10.1016/B978-0-12-814062-8.00002-9.
[4] Liu R, Wang Z, Sparks T, Liou F, Newkirk J. Aerospace applications of laser additive manufacturing. In: Laser additive manufacturing: materials, design, technologies, and applications. Elsevier Inc.; 2017. p. 351–71. 9780081004340.
[5] ASTM. International *ASTM 52911-1-19*. PA, USA: West Conshohocken; 2019.
[6] Aversa A, Marchese G, Saboori A, Bassini E, Manfredi D, Biamino S, Ugues D, Fino P, Lombardi M. New aluminum alloys specifically designed for laser powder bed fusion: a review. Materials 2019;12. https://doi.org/10.3390/ma12071007.
[7] Bourell D, Kruth JP, Leu M, Levy G, Rosen D, Beese AM, Clare A. Materials for additive manufacturing. CIRP Ann Manuf Technol 2017;66:659–81. https://doi.org/10.1016/j.cirp.2017.05.009.
[8] Padovano E, Badini C, Pantarelli A, Gili F, D'Aiuto F. A comparative study of the effects of thermal treatments on AlSi10Mg produced by laser powder bed fusion. J Alloys Compd 2020;831. https://doi.org/10.1016/j.jallcom.2020.154822.
[9] Weingarten C, Buchbinder D, Pirch N, Meiners W, Wissenbach K, Poprawe R. Formation and reduction of hydrogen porosity during selective laser melting of AlSi10Mg. J Mater Process Technol 2015;221:112–20. https://doi.org/10.1016/j.jmatprotec.2015.02.013.
[10] Hyer H, Zhou L, Park S, Gottsfritz G, Benson G, Tolentino B, McWilliams B, Cho K, Sohn Y. Understanding the laser powder bed fusion of AlSi10Mg alloy. Metallography, Microstructure, and Analysis 2020;9:484–502. https://doi.org/10.1007/s13632-020-00659-w.
[11] Kimura M, Hirayama A, Yoshioka J, Maekawa H, Kusaka M, Kaizu K, Takahashi T. Mechanical properties of AlSi12 alloy manufactured by laser powder bed fusion

technique. J Fail Anal Prev 2020;20:1884–95. https://doi.org/10.1007/s11668-020-00998-4.
[12] Ghasemi A, Fereiduni E, Balbaa M, Elbestawi M, Habibi S. Unraveling the low thermal conductivity of the LPBF fabricated pure Al, AlSi12, and AlSi10Mg alloys through substrate preheating. Addit Manuf 2022;59. https://doi.org/10.1016/j.addma.2022.103148.
[13] Vanzetti M, Virgillito E, Aversa A, Manfredi D, Bondioli F, Lombardi M, Fino P. Short heat treatments for the F357 aluminum alloy processed by laser powder bed fusion. Materials 2021;14. https://doi.org/10.3390/ma14206157.
[14] Aversa A, Marchese G, Manfredi D, Lorusso M, Calignano F, Biamino S, Lombardi M, Fino P, Pavese M. Laser powder bed fusion of a high strength Al-Si-Zn-Mg-Cu alloy. Metals 2018;8. https://doi.org/10.3390/met8050300.
[15] Rometsch PA, Zhu Y, Wu X, Huang A. Review of high-strength aluminium alloys for additive manufacturing by laser powder bed fusion. Mater Des 2022;219. https://doi.org/10.1016/j.matdes.2022.110779.
[16] Zhang X, Zheng H, Yu W. A review on solidification cracks in high-strength aluminum alloys via laser powder bed fusion. Mater Today Proc 2022;70:465–9. https://doi.org/10.1016/j.matpr.2022.09.366.
[17] Maamoun AH, Xue YF, Elbestawi MA, Veldhuis SC. The effect of selective laser melting process parameters on the microstructure and mechanical properties of Al6061 and AlSi10Mg alloys. Materials 2018;12. https://doi.org/10.3390/ma12010012.
[18] Tan Q, Liu Y, Fan Z, Zhang J, Yin Y, Zhang MX. Effect of processing parameters on the densification of an additively manufactured 2024 Al alloy. J Mater Sci Technol 2020;58:34–45. https://doi.org/10.1016/j.jmst.2020.03.070.
[19] Bradford RL, Cao L, Klosterman D, Herman F, Forman L, Browning C. A metal–metal powder formulation approach for laser additive manufacturing of difficult-to-print high-strength aluminum alloys. Mater Lett 2021;300. https://doi.org/10.1016/j.matlet.2021.130113.
[20] Montero Sistiaga ML, Mertens R, Vrancken B, Wang X, Van Hooreweder B, Kruth JP, Van Humbeeck J. Changing the alloy composition of Al7075 for better processability by selective laser melting. J Mater Process Technol 2016;238:437–45. https://doi.org/10.1016/j.jmatprotec.2016.08.003.
[21] Qi T, Zhu H, Zeng X, Yin J. Effect of Si content on the cracking behavior of selective laser melted Al7050. Rapid Prototyp J 2019;25:1592–600. https://doi.org/10.1108/RPJ-12-2018-0310.
[22] Uddin SZ, Murr LE, Terrazas CA, Morton P, Roberson DA, Wicker RB. Processing and characterization of crack-free aluminum 6061 using high-temperature heating in laser powder bed fusion additive manufacturing. Addit Manuf 2018;22:405–15. https://doi.org/10.1016/j.addma.2018.05.047.
[23] Zhang X, Zheng H, Yu W. A review on solidification cracks in high-strength aluminum alloys via laser powder bed fusion. Mater Today Proc 2022;70:465–9. https://doi.org/10.1016/j.matpr.2022.09.366.
[24] Martin JH, Yahata BD, Hundley JM, Mayer JA, Schaedler TA, Pollock TM. 3D printing of high-strength aluminium alloys. Nature 2017;549:365–9. https://doi.org/10.1038/nature23894.
[25] Schuster M, De Luca A, Widmer R, Maeder X, Leinenbach C Processability. Microstructure and precipitation of a Zr-modified 2618 aluminium alloy fabricated by laser powder bed fusion. J Alloys Compd 2022;913. https://doi.org/10.1016/j.jallcom.2022.165346.
[26] Mehta A, Zhou L, Huynh T, Park S, Hyer H, Song S, Bai Y, Imholte DD, Woolstenhulme NE, Wachs DM, et al. Additive manufacturing and mechanical properties of the dense and crack free Zr-modified aluminum alloy 6061 fabricated by the laser-powder bed fusion. Addit Manuf 2021;41. https://doi.org/10.1016/j.addma.2021.101966.
[27] Rosito M, Vanzetti M, Padovano E, Gili F, Sampieri R, Bondioli F, Badini CF. Processability of A6061 aluminum alloy using laser powder bed fusion by in situ synthesis of grain refiners. Metals 2023;13. https://doi.org/10.3390/met13061128.
[28] Wang P, Gammer C, Brenne F, Niendorf T, Eckert J, Scudino S. A heat treatable TiB2/Al-3.5Cu-1.5Mg-1Si composite fabricated by selective laser melting: microstructure, heat treatment and mechanical properties. Compos B Eng 2018;147:162–8. https://doi.org/10.1016/j.compositesb.2018.04.026.
[29] Li XP, Ji G, Chen Z, Addad A, Wu Y, Wang HW, Vleugels J, Van Humbeeck J, Kruth JP. Selective laser melting of nano-TiB2decorated AlSi10Mg alloy with high fracture strength and ductility. Acta Mater 2017;129:183–93. https://doi.org/10.1016/j.actamat.2017.02.062.
[30] Dai S, Zhang H, Bian Z, Geng J, Chen Z, Wang L, Wang M, Wang H. Insight into the recrystallization behavior and precipitation reaction of in-situ nano TiB2/Al[sbnd]Cu[sbnd]Mg composite during heat treatment. Mater Charact 2021;181. https://doi.org/10.1016/j.matchar.2021.111458.
[31] Xi L, Gu D, Guo S, Wang R, Ding K, Prashanth KG. Grain refinement in laser manufactured Al-based composites with TiB2 ceramic. J Mater Res Technol 2020;9:2611–22. https://doi.org/10.1016/j.jmrt.2020.04.059.
[32] Gu D, Yang Y, Xi L, Yang J, Xia M. Laser absorption behavior of randomly packed powder-bed during selective laser melting of SiC and TiB2 reinforced Al matrix composites. Opt Laser Technol 2019;119. https://doi.org/10.1016/j.optlastec.2019.105600.
[33] Karabulut Y, Ünal R. Additive manufacturing of ceramic particle-reinforced aluminum-based metal matrix composites: a review. J Mater Sci 2022;57:19212–42. https://doi.org/10.1007/s10853-022-07850-0.
[34] Li G, Zhao C, Huang Y, Tan Q, Hou J, He X, Guo C, Lu W, Zhou L, Liu S, et al. Additively manufactured fine-grained ultrahigh-strength bulk aluminum alloys with nanostructured strengthening defects. Mater Today 2024;76:40–51. https://doi.org/10.1016/j.mattod.2024.05.006.
[35] Zhu Z, Ng FL, Seet HL, Lu W, Liebscher CH, Rao Z, Raabe D, Mui Ling Nai S. Superior mechanical properties of a selective-laser-melted AlZnMgCuScZr alloy enabled by a tunable hierarchical microstructure and dual-nanoprecipitation. Mater Today 2022;52. https://doi.org/10.1016/j.mattod.2021.11.019.
[36] Sharma DK, Mahant D, Upadhyay G. Manufacturing of metal matrix composites: a state of review. Proceedings of the Materials Today: Proceedings; Elsevier Ltd 2019;26:506–19.
[37] Tan Q, Zhang M. Recent advances in inoculation treatment for powder-based additive manufacturing of aluminium alloys. Mater Sci Eng R Rep 2024;158.
[38] Torbati-Sarraf H, Torbati-Sarraf SA, Chawla N, Poursaee A. A comparative study of corrosion behavior of an additively manufactured Al-6061 RAM2 with extruded Al-6061 T6. Corros Sci 2020;174. https://doi.org/10.1016/j.corsci.2020.108838.
[39] Sullivan E, Polizzi A, Iten J, Nuechterlein J, Domack M, Liu S. Microstructural characterization and tensile behavior of reaction synthesis aluminum 6061 metal matrix composites produced via laser beam powder bed fusion and electron beam freeform fabrication. Int J Adv Manuf Technol 2022;121:2197–218. https://doi.org/10.1007/s00170-022-09443-2.
[40] Koutny D, Palousek D, Pantelejev L, Hoeller C, Pichler R, Tesicky L, Kaiser J. Influence of scanning strategies on processing of aluminum alloy EN AW 2618 using selective laser melting. Materials 2018;11. https://doi.org/10.3390/ma11020298.
[41] Belelli F, Casati R, Larini F, Riccio M, Vedani M. Investigation on two Ti–B-reinforced Al alloys for laser powder bed fusion. Mater Sci Eng 2021;808. https://doi.org/10.1016/j.msea.2021.140944.
[42] Belelli F, Casati R, Riccio M, Rizzi A, Kayacan MY, Vedani M. Development of a novel high-temperature al Alloy for laser powder bed fusion. Metals 2021;11:1–12. https://doi.org/10.3390/met11010035.
[43] Liu X, Liu Y, Zhou Z, Luo W, Zeng Z. Enhanced printability and strength of unweldable aa2024-based nanocomposites fabricated by laser powder bed fusion via nano-TiC-induced grain refinement. Materials Science and Engineering: A 2022;856. https://doi.org/10.1016/j.msea.2022.144010.
[44] Aversa A, Moshiri M, Librera E, Hadi M, Marchese G, Manfredi D, Lorusso M, Calignano F, Biamino S, Lombardi M, et al. Single scan track analyses on aluminium based powders. J Mater Process Technol 2018;255:17–25. https://doi.org/10.1016/j.jmatprotec.2017.11.055.
[45] Bosio F, Aversa A, Lorusso M, Marola S, Gianoglio D, Battezzati L, Fino P, Manfredi D, Lombardi M. A time-saving and cost-effective method to process alloys by laser powder bed fusion. Mater Des 2019;181. https://doi.org/10.1016/j.matdes.2019.107949.
[46] Maxime Delmée. Mertz grégory functionalized metal powders by small particles made by non-thermal plasma glow discharge for additiive manufacturing applications. 2019. p. 1–24.
[47] ASTM International ASTM. B822 - 20 standard test method for particle size distribution of metal powders and related compounds by light scattering. PA, USA: West Conshohocken; 2020.
[48] Mindt HW, Megahed M, Lavery NP, Holmes MA, Brown SGR. Powder bed layer characteristics: the overseen first-order process input. Metall Mater Trans A Phys Metall Mater Sci 2016;47:3811–22. https://doi.org/10.1007/s11661-016-3470-2.
[49] Martucci A, Marinucci F, Sivo A, Aversa A, Manfredi D, Bondioli F, Fino P, Lombardi M. An automatic on top analysis of single scan tracks to evaluate the laser powder bed fusion building parameters. Materials 2021;14. https://doi.org/10.3390/ma14185171.
[50] Nie X, Zhang H, Zhu H, Hu Z, Ke L, Zeng X. Analysis of processing parameters and characteristics of selective laser melted high strength Al-Cu-Mg alloys: from single tracks to cubic samples. J Mater Process Technol 2018;256:69–77. https://doi.org/10.1016/j.jmatprotec.2018.01.030.
[51] Mercurio V, Calignano F, Iuliano L. Sustainable production of AlSi10Mg parts by laser powder bed fusion process. Int J Adv Manuf Technol 2023;125:3117–33. https://doi.org/10.1007/s00170-023-11004-0.
[52] Parveen, S.; Umamaheswar Rao, R.S.; Divya, K.; Telesang, G. Investigation on correlation between microstructure and mechanical properties of AlSi10Mg specimens by AM technology.
[53] Dadkhah M, Mosallanejad MH, Iuliano L, Saboori A. A comprehensive overview on the latest progress in the additive manufacturing of metal matrix composites: potential, challenges, and feasible solutions. Acta Metall Sin 2021;34:1173–200. https://doi.org/10.1007/s40195-021-01249-7.
[54] Lüddecke A, Pannitz O, Zetzener H, Sehrt JT, Kwade A. Powder properties and flowability measurements of tailored nanocomposites for powder bed fusion applications. Mater Des 2021;202. https://doi.org/10.1016/j.matdes.2021.109536.
[55] Sun X, Chen M, Liu T, Zhang K, Wei H, Zhu Z, Liao W. Characterization, preparation, and reuse of metallic powders for laser powder bed fusion: a review. Int J Extrem Manuf 2024;6.
[56] Li G, Huang Y, Li X, Guo C, Zhu Q, Lu J. Laser powder bed fusion of nano-titania modified 2219 aluminium alloy with superior mechanical properties at both room and elevated temperatures: the significant impact of solute. Addit Manuf 2022;60. https://doi.org/10.1016/j.addma.2022.103296.
[57] Li G, Li X, Guo C, Zhou Y, Tan Q, Qu W, Li X, Hu X, Zhang MX, Zhu Q. Investigation into the effect of energy density on densification, surface roughness and loss of alloying elements of 7075 aluminium alloy processed by laser powder bed fusion. Opt Laser Technol 2022;147. https://doi.org/10.1016/j.optlastec.2021.107621.
[58] Yi J, Zhang X, Liu G, Rao JH, Liu H. Microstructure and dynamic microhardness of additively manufactured (TiB2+TiC)/AlSi10Mg composites with AlSi10Mg and B4C coated Ti powder. J Alloys Compd 2023;939. https://doi.org/10.1016/j.jallcom.2023.168718.

[59] Gao C, Xiao Z, Liu Z, Zhu Q, Zhang W. Selective laser melting of nano-TiN modified AlSi10Mg composite powder with low laser reflectivity. Mater Lett 2019;236. https://doi.org/10.1016/j.matlet.2018.10.126.
[60] Balbaa MA, Ghasemi A, Fereiduni E, Elbestawi MA, Jadhav SD, Kruth JP. Role of powder particle size on laser powder bed fusion processability of AlSi10mg alloy. Addit Manuf 2021;37. https://doi.org/10.1016/j.addma.2020.101630.
[61] Bidulsky R, Gobber FS, Bidulska J, Ceroni M, Kvackaj T, Grande MA. Coated metal powders for laser powder bed fusion (L-PBF) processing: a review. Metals 2021;11.
[62] Chi J, Shao H, Song H, Wang X, Wu K, Zheng Q, Dmitrievich Starostenkov M, Dong G, Bi J. Effect of double-pulse frequency and post-weld heat treatment on microstructure and mechanical properties of metal-inert gas welded Al–Mg–Si alloy joints. Materials Science and Engineering: A 2024;913. https://doi.org/10.1016/j.msea.2024.147029.
[63] Chi J, Bi J, Zheng J, Zou J, Wu L, Zheng Q, Lu N, Starostenkov MD, Dong G, Han J, et al. Rapidly modifying microstructure via electro pulsing treatment for AA2219 laser welded joints: synergistic enhancement of strength, ductility, and corrosion resistance. J Manuf Process 2024;131:2365–81. https://doi.org/10.1016/j.jmapro.2024.10.045.
[64] Bi J, Chi J, Song H, Shao H, Wang K, Yang Z, Jia X, Dong G. Enhancing tensile properties of MIG welded AA6061 joints: effect of pulse mode and post-weld heat treatment. Mater Today Commun 2024;39. https://doi.org/10.1016/j.mtcomm.2024.109156.
[65] Niel A, Bordreuil C, Deschaux-Beaume F, Fras G. Modelling hot cracking in 6061 aluminium alloy weld metal with microstructure based criterion. Sci Technol Weld Join 2013;18. https://doi.org/10.1179/1362171812Y.0000000072.
[66] Hagenlocher C, Seibold M, Weber R, Graf T. Modulation of the local grain structure in laser beam welds to inhibit the propagation of centerline hot cracks. Proceedings of the procedia CIRP, vol. 74; 2018.
[67] Drezet JM, Lima MSF, Wagnière JD, Rappaz M, Kurz W. Crack-free aluminium alloy welds using a twin laser process. Weld World 2008;52.
[68] Albannai AI, Aloraier AS, Alaskari AM, Alawadhi MY. Improving centerline solidification crack resistivity of AA 2024 using tandem side-by-side GTAW technique. Mater Perform Charact 2019;8. https://doi.org/10.1520/MPC20180110.
[69] Sonawane A, Roux G, Blandin JJ, Despres A, Martin G. Cracking mechanism and its sensitivity to processing conditions during laser powder bed fusion of a structural aluminum alloy. Materialia (Oxf) 2021;15. https://doi.org/10.1016/j.mtla.2020.100976.
[70] Sonawane A, Roux G, Blandin J-J, Despres A, Martin G. Insights into the cracking mechanism affecting a structural aluminum alloy processed by laser powder bed fusion. SSRN Electron J 2020. https://doi.org/10.2139/ssrn.3693574.
[71] Lo YL, Liu BY, Tran HC. Optimized hatch Space selection in double-scanning track selective laser melting process. Int J Adv Manuf Technol 2019;105:2989–3006. https://doi.org/10.1007/s00170-019-04456-w.
[72] Wang D, Yang Y, Su X, Chen Y. Study on energy input and its influences on single-Track,Multi-track, and multi-layer in SLM. Int J Adv Manuf Technol 2012;58:1189–99. https://doi.org/10.1007/s00170-011-3443-y.
[73] Jang HS, Kim SH, Park GW, Jeon JB, Kim D, Kim D, Kim WR, Choi YS, Shin S. Process parameter optimization for laser powder bed fusion of Fe-Si alloy considering surface morphology and track width of single scan track. Materials 2023;16. https://doi.org/10.3390/ma16247626.
[74] Tang C, Le KQ, Wong CH. Physics of humping formation in laser powder bed fusion. Int J Heat Mass Transf 2020;149. https://doi.org/10.1016/j.ijheatmasstransfer.2019.119172.
[75] Zheng H, Li H, Lang L, Gong S, Ge Y. Effects of scan speed on vapor plume behavior and spatter generation in laser powder bed fusion additive manufacturing. J Manuf Process 2018;36:60–7. https://doi.org/10.1016/j.jmapro.2018.09.011.
[76] Karabulut Y, Ünal R. Additive manufacturing of ceramic particle-reinforced aluminum-based metal matrix composites: a review. J Mater Sci 2022;57:19212–42.
[77] Tang C, Le KQ, Wong CH. Physics of humping formation in laser powder bed fusion. Int J Heat Mass Transf 2020;149. https://doi.org/10.1016/j.ijheatmasstransfer.2019.119172.
[78] Li E, Zhou Z, Wang L, Zou R, Yu A. Numerical studies of melt pool and gas bubble dynamics in laser powder bed fusion process. Addit Manuf 2022;56. https://doi.org/10.1016/j.addma.2022.102913.
[79] Bhatt A, Huang Y, Leung CLA, Soundarapandiyan G, Marussi S, Shah S, Atwood RC, Fitzpatrick ME, Tiwari MK, Lee PD. In situ characterisation of surface roughness and its amplification during multilayer single-track laser powder bed fusion additive manufacturing. Addit Manuf 2023;77. https://doi.org/10.1016/j.addma.2023.103809.
[80] Guo C, Li S, Shi S, Li X, Hu X, Zhu Q, Ward RM. Effect of processing parameters on surface roughness, porosity and cracking of as-built IN738LC parts fabricated by laser powder bed fusion. J Mater Process Technol 2020;285. https://doi.org/10.1016/j.jmatprotec.2020.116788.
[81] Yang KV, Shi Y, Palm F, Wu X, Rometsch P. Columnar to equiaxed transition in Al-Mg(-Sc)-Zr alloys produced by selective laser melting. Scr Mater 2018;145:113–7. https://doi.org/10.1016/j.scriptamat.2017.10.021.